Space Weather

RESEARCH ARTICLE
10.1029/2023SW003605

Investigation of Ionospheric Small-Scale Plasma Structures Associated With Particle Precipitation

F. Enengl[1], L. Spogli[2,3], D. Kotova[1], Y. Jin[1], K. Oksavik[4,5], N. Partamies[5], and W. J. Miloch[1]

[1]Department of Physics, University of Oslo, Oslo, Norway, [2]Istituto Nazionale di Geofisica e Vulcanologia, Rome, Italy, [3]SpacEarth Technology, Rome, Italy, [4]Birkeland Centre for Space Science, Department of Physics and Technology, University of Bergen, Bergen, Norway, [5]Arctic Geophysics, University Centre in Svalbard, Longyearbyen, Norway

Key Points:

- Enhanced values of the GNSS-based 1–s amplitude scintillation index are observed at auroral intensity gradients
- The IFLC is often elevated at the same time as the S4 index, confirming the diffractive nature of observed scintillation events
- Significant increases in the auroral particle precipitation result in joint signatures of increased ionospheric currents and plasma structuring below the Fresnel's scale

Supporting Information:

Supporting Information may be found in the online version of this article.

Correspondence to:

F. Enengl,
florine.enengl@fys.uio.no

Citation:

Enengl, F., Spogli, L., Kotova, D., Jin, Y., Oksavik, K., Partamies, N., & Miloch, W. J. (2024). Investigation of ionospheric small-scale plasma structures associated with particle precipitation. *Space Weather*, *22*, e2023SW003605. https://doi.org/10.1029/2023SW003605

Received 16 JUN 2023
Accepted 11 DEC 2023

Abstract We investigate the role of auroral particle precipitation in small-scale (below hundreds of meters) plasma structuring in the auroral ionosphere over the Arctic. In this scope, we analyze together data recorded by an Ionospheric Scintillation Monitor Receiver (ISMR) of Global Navigation Satellite System (GNSS) signals and by an All-Sky Imager located in Longyearbyen, Svalbard (Norway). We leverage on the raw GNSS samples provided at 50 Hz by the ISMR to evaluate amplitude and phase scintillation indices at 1 s time resolution and the Ionosphere-Free Linear Combination at 20 ms time resolution. The simultaneous use of the 1 s GNSS-based scintillation indices allows identifying the scale size of the irregularities involved in plasma structuring in the range of small (up to few hundreds of meters) and medium-scale size ranges (up to few kilometers) for GNSS frequencies and observational geometry. Additionally, they allow identifying the diffractive and refractive nature of fluctuations on the recorded GNSS signals. Six strong auroral events and their effects on plasma structuring are studied. Plasma structuring down to scales of hundreds of meters is seen when strong gradients in auroral emissions at 557.7 nm cross the line of sight between the GNSS satellite and receiver. Local magnetic field measurements confirm small-scale structuring processes coinciding with intensification of ionospheric currents. Since 557.7 nm emissions primarily originate from the ionospheric E-region, plasma instabilities from particle precipitation at E-region altitudes are considered to be responsible for the signatures of small-scale plasma structuring highlighted in the GNSS scintillation data.

Plain Language Summary We investigate the role of auroral particle precipitation in plasma structuring in the auroral ionosphere over the Arctic. For this we use Ionospheric Scintillation Monitor Receiver of Global Navigation Satellite System (GNSS) signals to detect plasma structuring and an All-Sky- Camera to monitor the Aurora. Six strong auroral events are studied. Plasma structuring down to scales of hundreds of meters are seen when strong gradients in green auroral emissions cross the line of sight between the GNSS satellite and receiver. Intensification of ionospheric currents are observed to coincide with small-scale structuring processes. Green auroral emissions originate from the ionospheric E-region, which is considered the source of plasma instabilities causing the signatures of small-scale plasma structuring as observed in the GNSS scintillation data.

1. Introduction

Particle precipitation into the E and F-region ionosphere can cause plasma irregularities and structuring on various scales (Alfonsi et al., 2022; Dahlgren et al., 2017; De Franceschi et al., 2019; Enengl et al., 2023; Fæhn Follestad et al., 2020; Jin et al., 2016; Moen et al., 2013; Urbar et al., 2022; van der Meeren et al., 2015; Zou et al., 2013). As radio waves propagate through the ionosphere they undergo diffraction and refraction (Huba et al., 1985; Keskinen & Ossakow, 1983; Kintner & Seyler, 1985). This can result in rapid fluctuations of the phase and amplitude as observed by ground-based receivers (Hey et al., 1946; Kintner et al., 2007). Irregularities below the Fresnel's scale result in diffractive effects in the amplitude and phase of signals recorded on ground. The Fresnel's scale for Global Navigation Satellite System (GNSS) frequencies and observational geometry is in the order of a few hundreds of meters. In fact, those small-scale irregularities are the primary source of scintillation: they act as a new wave source for the GNSS planar waves and cause interference at the receiver level (Basu et al., 1998; Kintner et al., 2007; Wernik et al., 2003). Recent literature highlighted that fluctuations of this kind are the only one deemed to be called "scintillation" because of the stochastic nature of the induced fluctuations (Ghobadi et al., 2020; McCaffrey & Jayachandran, 2019). Besides scintillation, fluctuations on the GNSS phase measurements are due to irregularities covering the full range of scales. These fluctuations are deterministic in

nature (McCaffrey & Jayachandran, 2019). In fact, above the Fresnel scale, changes in the ionosphere's refractive index lead to refraction. Within this scale range, the rate of total electron content (TEC) change index (ROTI) has recently been shown by Rino et al. (2019) to give some good hints about possible stochastic features of ionospheric effects caused by large-scale and medium-scale structures. Most of the recent research on the GNSS scintillation has been dedicated to efficiently evaluate the diffractive and refractive contribution in the recorded GNSS fluctuations, especially in the high-latitude ionosphere, where the highly dynamic plasma complicates such a task (Conroy et al., 2022; Ghobadi et al., 2020; McCaffrey & Jayachandran, 2019; Spogli et al., 2021; Wang et al., 2018, 2022). In this study, we investigate the role of the particle precipitation in small-scale plasma structuring in the E and F-region ionosphere and its effects on trans-ionospheric radio wave propagation over Svalbard (Norway).

One visual signature of ionosphere-magnetosphere coupling through the Birkeland currents is the aurora. Using all-sky imagers with filters for the green and red auroral emission lines gives an indication of the location and altitude of the particle precipitation energy deposition. As the geomagnetic activity grows, particle precipitation leads to brighter aurora. Auroral emissions indicate particle precipitation into the E and F-region altitudes; green (557.7 nm) emissions correspond primarily to E-region altitudes, with the maximum emission altitude at ca. 114 km (Whiter et al., 2023), and the red (630.0 nm) emissions to F-region altitudes, with a peak above 300 km altitude. Different emissions are also related to energies of precipitating electrons. Electrons of energies >5 keV frequently precipitate down to the E-region of the ionosphere, where they deposit their energy (Dimant et al., 2021). The maximum height of energy deposition rate of particles at energies of 5 keV is at 115 km, while for particles at energies of 10 keV at 105 km, thus within the E-region of the ionosphere (Brekke, 2013). Such energies of the precipitating electrons are typical for the auroral oval, but even much higher energies can be reached during the geomagnetic storms and substorms.

The influx of energetic particles leads to increased plasma density and enhanced conductance in the ionosphere. In addition, the electric fields are mapped from the magnetosphere into the ionosphere. The ionosphere is then characterized by plasma drifts/flows and structuring. Instabilities associated with auroral particle precipitation are kinetic instabilities, such as the two-stream instabilities or current-driven instabilities (Kropotkin, 2016). Neutrals are also present in the E-region ionosphere, which provides favorable conditions for the Farley-Buneman instability that arises from the difference between the electron and ion velocities, which is due to high rate of collisions between ions and neutrals (Buneman, 1963; Farley Jr, 1963; Rogister & D'Angelo, 1970; Treumann, 1997). Given the impacts of particle streams onto ionospheric plasma conditions, particle precipitation is proposed to contribute to ionospheric small-scale plasma structuring (Greenwald et al., 2002).

Ionospheric plasma structuring can be indirectly observed by Ionospheric Scintillation Monitor Receivers (ISMRs). The above mentioned phase and amplitude fluctuations are usually studied through the phase (σ_Φ) and amplitude (S4) scintillation indices. As anticipated above, phase scintillations are driven by ionospheric irregularities at small wave numbers and below the first Fresnel's radius for the GNSS frequencies and observational geometry. Note that σ_Φ values can also be impacted by the selected data filtering with respect to fast flows. Phase scintillation below the first Fresnel radius is the result of interference between different phases and can be thought of as diffractive, while phase scintillation at small wave numbers is considered refractive and produced by fluctuations of plasma density integrated along the signal path (Kintner et al., 2007). However, the overall phase fluctuations measured at ground can be split into a refractive and diffractive contribution. The refractive part of the signal is deterministic, as it can be related to the electron density and wave frequency and can be accounted for. The diffractive part is stochastic (Kintner et al., 2007; McCaffrey & Jayachandran, 2019). Amplitude scintillations are related to diffractive effects, as the refraction impacts the wave path and power but will not cause amplitude fluctuations (McCaffrey & Jayachandran, 2019). Refraction is observed for small and large scale structures, while diffraction occurs due to structures equal to or below the Fresnel's scale (Kintner et al., 2007; Zheng et al., 2022). The first order refractive contribution to GNSS phase fluctuations can be accounted for by calculating the Ionosphere-Free Linear Combination (IFLC) (Carrano et al., 2013). The IFLC is a combination of the carrier phases of two received waves at different frequencies, which is able to account for the bulk of the refractive contribution induced by the ionosphere on the phase measurements (McCaffrey & Jayachandran, 2019). The use of the IFLC has been recently adopted to improve the phase detrending scheme used to evaluate the phase scintillation index. In fact, phase detrending is a delicate issue for ISMRs located in the high-latitude regions (Beach, 2006; Forte, 2005), for which the standard detrending scheme based on the 6th-order Butterworth high-pass filter with the cutoff frequency of 0.1 Hz is not effective in eliminating the bulk of the refractive contributions above the Fresnel's scale. To address this issue, the Fast Iterative Filtering technique

(Cicone, 2020; Cicone & Zhou, 2021) was recently used to determine a more suitable and adaptive detrending scheme, with related cutoff frequency, to provide a phase scintillation index in which the bulk of the refractive part is eliminated (Ghobadi et al., 2020; Spogli et al., 2021). Bearing this in mind, it depends on the purpose and whether one is interested in the refractive contributions as a proxy for plasma structuring to decide on the choice of indices and on the related detrending scheme for the GNSS phase measurements. Investigating the IFLC and scintillation indices together with the temporal and spatial evolution of particle precipitation, may improve our understanding of when/where small-scale structures are present, their role in plasma structuring and what their nature is.

Previous studies have already laid a pathway to understand the occurrence of ionospheric irregularities in relation to particle precipitation and their impact on trans-ionospheric radio wave propagation at high latitudes. The control of the interplanetary magnetic field (IMF) extends to small-scale irregularities of plasma density associated with the large-scale structures in the ionosphere. For IMF Bz northward conditions moderate levels of amplitude and phase scintillation were observed with highly variable decorrelation times (Basu et al., 1991). The relationship between auroral particle precipitation, electric fields and ionospheric irregularities is a result of magnetosphere-ionosphere coupling. It confirms the dependence of ionospheric plasma instabilities on electric fields and precipitation-induced electron density gradients (Greenwald et al., 2002). Meso-scale electron density irregularities on the dayside auroral region are found pole-ward of the nominal cusp region (Basu et al., 1998). Irregularities on the pole-ward side of the aurora are predominantly smaller than the Fresnel scale (observed as amplitude scintillation) (Conroy et al., 2022). Plasma structuring as driven by particle precipitation is proposed to be driven at the boundaries of the auroral precipitation (by such instabilities as Kelvin-Helmholtz and/or Farley-Buneman) down to E-region altitudes and to play a main role in plasma structuring on various scales (Enengl et al., 2023). Pole-ward moving auroral forms can cause stronger ionospheric irregularities, capable of causing more severe disturbances in the cusp ionosphere for navigation signals than polar cap patches (Oksavik et al., 2015). Loss of lock events appeared consistently at the edges of an auroral form named the westward traveling surge in a study by Semeter et al. (2017). The authors concluded that the E-region (near the 557.7 nm oxygen emission peak altitude) was the source of the irregularities.

Moving auroral structures in the E-region occurred simultaneously with the Global Positioning System (GPS) signals showing the movement of the ionospheric regions causing diffractive fading as observed by Smith et al. (2008). Refraction and diffraction occur simultaneously during scintillation (Zheng et al., 2022). Zheng et al. (2022) observed that IFLC, S4 and phase indices showed consistent fluctuations for most of scintillation events. However, they observed that IFLC and S4 did not always simultaneously correspond to scintillations, as IFLC was enhanced during the geomagnetic storm and S4 was not. They suggested that IFLC during the geomagnetic storm is caused by the increased high-frequency phase power, which is related to the enhanced density of small-scale irregularities during storm periods.

The following questions still remain open: (a) how do spatial and temporal characteristics of small-scale structures relate to the auroral emissions? (b) how does particle precipitation contribute to Fresnel's scale structuring? In this work, we study how small-scale plasma structuring is spatially and temporally related to the auroral particle precipitation. The effects of small-scale structuring on trans-ionospheric radio wave propagation are used to investigate times of elevated scintillation indices and understand the plasma conditions and generation of small-scale structures. To quantify small-scale structuring processes, we use scintillation indices. For the auroral precipitation, we measure the auroral intensity at different emission lines.

2. Approach and Data Selection

The scintillation indices used in this study are the amplitude scintillation index (S4) and the phase scintillation index (σ_ϕ) (Fremouw et al., 1978). We further use the ionosphere-free linear combination (IFLC). The scintillation indices and IFLC are calculated using amplitude and phase, which in ISMRs are usually sampled at 50–100 Hz rate for each satellite in the field of view. The considered ISMR is a Septentrio PolaRxS/PolaRx5s multi-frequency multi-constellation receiver (Bougard et al., 2011) operated by the Istituto Nazionale di Geofisica e Vulcanologia (INGV, Italy) and situated at Longyearbyen, Svalbard (geographic coordinates: 78.17°N, 15.99°E). The receiver is operational since January 2019 and the scintillation data provided are part of the scintillation data collection (Upper atmosphere physics and radiopropagation Working Group et al., 2020) available in the electronic Space Weather Upper atmosphere (eSWua, eswua.ingv.it) data portal. In this study, we concentrate on data from the GPS and Galileo constellations. GPS satellites are indicated by G followed by their PRN code (e.g., G01), and Galileo satellites by E followed by their PRN code (e.g., E01). The cut-off angle

to avoid multipath effects is set to 35°. Scintillation indices and IFLC are then derived according to equations presented below (Carrano et al., 2013; de Paula et al., 2021; Yeh & Liu, 1982).

The signal intensity I is calculated using the signal amplitude A:

$$I = A^2 = I_c^2 + Q_c^2, \tag{1}$$

with I_c and Q_c being the signal intensity in-phase and quadrature components (Briggs & Parkin, 1963; Van Dierendonck et al., 1993; Yeh & Liu, 1982). I is then detrended using a 6th-order high-pass Butterworth filter, with a cutoff frequency of 0.1 Hz. The amplitude scintillation index S_4 is then given by:

$$S_4 = \sqrt{\frac{\langle I^2 \rangle - \langle I \rangle^2}{\langle I \rangle^2}}. \tag{2}$$

The phase was detrended with a 6th-order high-pass Butterworth filter, with a cutoff frequency of 0.1 Hz, and the accumulated phase was calculated by $2\pi\phi_c$, with ϕ_c being the carrier phase. Subsequently, the phase scintillation index σ_ϕ is calculated by:

$$\sigma_\phi = \sqrt{\langle \phi^2 \rangle - \langle \phi \rangle^2}, \tag{3}$$

as the standard deviation of the detrended measured phase (Kintner et al., 2007; Yeh & Liu, 1982).

ISMRs traditionally have a firmware able to provide the scintillation indices in quasi real-time with a 1 min time resolution (running window). For the purpose of our work, we decided to consider scintillation data at a better time resolution, that is, use a shorter running window of 1 s. Functions used to calculate the S_4 and σ_ϕ index, with a running window of 1 s (50 data points, due to the 50 Hz sampling resolution), are shown in Supporting Information S1. Such an approach has been proven to be more effective in detecting small-scale irregularities triggered by the auroral particle precipitation (Materassi & Mitchell, 2007; Wang et al., 2021), which are otherwise almost absent when considered on the standard 1-min basis (see, e.g., the climatological results provided in Alfonsi et al. (2011), De Franceschi et al. (2019), Moen et al. (2013), and Spogli et al. (2009)). According to what is reported in Forte and Radicella (2002) and in their Equations 6 and 7, some scintillation indices at 1 s allow studying spatial scales of the irregularities that are below 100 m, that is, below the Fresnel's scale, and are able to account for spatial variability of particle precipitation patterns. For an overview of which indices allow monitoring at small, medium or large scale ranges, see Mrak et al. (2023).

When a GNSS signal propagates through the ionosphere, refraction occurs. The phase delay caused by this refraction is given as the refractive index ionospheric correction term R_{corr}:

$$R_{corr} = \frac{40.3}{f_c^2} \int n_e dL, \tag{4}$$

with f being the signal carrier frequency and the electron density n_e is integrated along the raypath dL (Kashcheyev et al., 2012; Zheng et al., 2022). For propagation paths, which are assumed to be the same for different carrier frequencies, the R_{corr} ratio of two carrier waves is given by

$$\frac{R_{corr1}}{R_{corr2}} = \frac{f_1^2}{f_2^2}. \tag{5}$$

Carrier phase variations L_ϕ at a constant frequency are given by

$$L_\phi = r + \lambda N - R_{corr}, \tag{6}$$

with the signal wavelength λ, integer ambiguity N, and the geometric distance r. The ionosphere-free linear combination is then calculated by:

$$IFLC = \frac{f_1^2 \phi_{L1} - f_2^2 \phi_{L2}}{f_1^2 - f_2^2} = r + \frac{f_1^2}{f_1^2 - f_2^2} \lambda N - \frac{f_2^2}{f_1^2 - f_2^2} \lambda N, \tag{7}$$

with the two carrier frequencies f_1 and f_2 and the corresponding carrier phases ϕ_{L1} and ϕ_{L2}. The ionospheric refractive index correction term R_{corr} is now removed and the IFLC is non-refractive (Carrano et al., 2013; Cordes

Table 1
Selected Particle Precipitation Events

#	Date	Precipitation signature	Shown in
1	24th October 2019	Long	Figure 1
2	28th October 2019	Long	Figure 2
3	29th October 2019	Long	Figure 2
4	6th November 2019	Short	Figure 1
5	7th November 2019	Long	Figure 2
6	22nd February 2020	Short	Figure 3

et al., 1986; McCaffrey & Jayachandran, 2019; Zheng et al., 2022). The IFLC is then considered at the same rate of the I_c and Q_c samples, that is, 50 Hz.

In this work, the auroral emissions were captured by an all-sky imager (ASI): Keo Sentry 4ix Monochromatic Imager from KEO Scientific, operated by the University of Oslo (Norway) situated in Longyearbyen Svalbard (geographic coordinates: 78.15°N, 16.04°E). The imager is equipped with narrow band-pass filters to monitor 557.7 nm (green) and 630.0 nm (red) auroral emissions, recording images every 15–30 s. The green auroral emissions are projected to an altitude of 150 km (Enengl et al., 2023; Partamies et al., 2022). The red auroral images were projected to an altitude of 250 km. Observations of the brightest aurora may be influenced by the way the camera is operated and calibrated. These observations are nevertheless a good measure for a comparison between the auroral activity and the σ_ϕ indices.

In this article, we focus on the time period of 2019–2020 (during a solar minimum) the first season where the ISMR was operational. The availability of clear all-sky, auroral images of intense particle precipitation, and simultaneous scintillation receiver data is the first filtering stage of our data set.

Subsequently, we filter for a Kp index larger than 1+ and solar wind speeds exceeding 400 km/s, to ensure ongoing geomagnetic activity. The geomagnetic and solar wind parameters were downloaded from the NASA/GSFC's OMNI data set through OMNIWeb (King & Papitashvili, 2005).

Further, all events show moderate local deflections in the horizontal magnetic field H component (over 100 nT). The H component is recorded by a magnetometer network around Svalbard operated by the Tromsø Geophysical Observatory (Tanskanen, 2009). The signature of the enhancement of the westward electrojet and the substorm current wedge in superposition with eastward electrojet enhancements is imprinted as a decrease in the H component of the magnetic field at high latitudes (Akasofu, 1965; D'Onofrio et al., 2014). Six events, which are summarized in Table 1, fulfill these criteria and are studied in detail.

3. Observations

The six strong auroral particle precipitation events are analyzed in the context of scintillation indices and magnetometer data indicating structuring processes and geomagnetic conditions. Figure 1 presents the two event types we encountered: long-lasting and short-lived precipitation events (Figures 1c and 1h, respectively). Here, the first detected long-lasting and short-lived event are shown side by side to study the differences. Later, the remaining events of each category are discussed. The data from 24th October 2019 (#1) to 6th November 2019 (#4) show increased S4 index valued (Figures 1a and 1f), indicating plasma structuring below Fresnel's scale. Peaks in S4 index values (shown by black arrows in Figures 1a and 1f) are recorded at: 16:18 UT, 16:20 UT, 16:31 UT, 16:48 UT on 24th October 2019 (#1) and 19:00 UT, 19:18 UT, 19:22 UT, 19:26 UT, 19:44 UT, 19:50 UT on 6th November 2019 (#4). To investigate the nature and cause of these elevated S4 observations, the IFLC, auroral intensity (I), σ_ϕ and H component are investigated. The peaks corresponding to elevated S4 indices are marked for all parameters in all panels by black arrows. The IFLC is shown in Figures 1b and 1g. Besides the elevated noise level at the beginning of both event windows, correspondence between S4 and IFLC is observed for the elevated S4 values. The IFLC indicates a diffractive contribution to scintillation. The auroral intensity at the ionospheric piercing point of the signal path of the satellite at the auroral emission plane is presented in Figures 1c and 1h. Here, we can observe the key difference between the two events: the 24th October 2019 (#1) event has an onset of auroral particle precipitation around 16:15 UT and stays above 15 kR auroral intensity for the period from 16:20 UT to 16:48 UT. The 6th November 2019 (#4) event shows multiple peaks in the auroral intensity at around 19:00 UT, 19:18 UT, 19:21 UT, 19:25 UT, 19:42 UT, 19:47 UT. All of them are happening in a close minute window of the S4 index peaks, shortly before or after. The σ_ϕ index is shown in Figures 1d and 1i and it can be interpreted as a measure of small and large-scale structuring in the ionosphere. The elevations in the σ_ϕ index are roughly co-located with the elevated S4 index, however not all of the σ_ϕ variations can be associated with S4 index variations, for example, on 24th October 2019 (#1) 16:35 UT. The vertical lines at the last intensity peaks of the particle precipitation signatures spanning over multiple panels, shows the ongoing elevation in the scintillation indices. The indices can stay elevated for some time after the particle precipitation declines or moves. The variation in the H component of the magnetic field is a measure for substorm activity, shown in Figures 1e and 1j. The H component decreases at

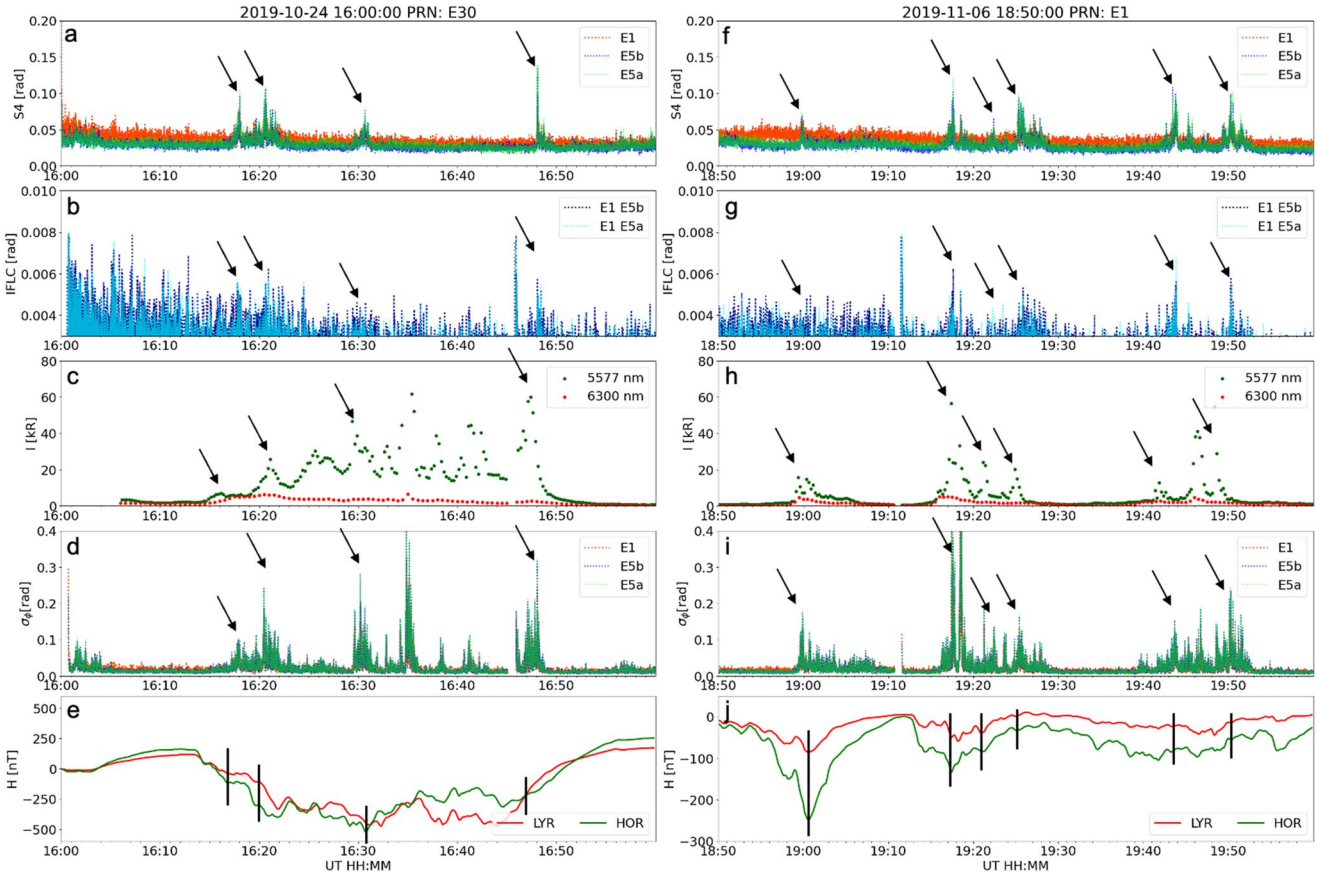

Figure 1. Small-scale plasma structures during particle precipitation. The data from 24th October 2019 (#1) and 6th November 2019 (#4) show observations of scintillation indices (S4—panel a and f; σ_ϕ—panel d and i), the IFLC (panel b and g), magnetometer data (panel e and j), and auroral intensity (panel c and h). The peaks in S4 and IFLC mark strong intensity gradients (e.g., commence and end) of the elevated auroral intensity during strongly negative *H*, suggesting small-scale structuring during the commence and fading of particle precipitation. Most S4 peaks are accompanied by elevated σ_ϕ, indicating simultaneous large and small-scale structuring. The last auroral intensity peaks of the particle precipitation signature are highlighted by vertical lines spanning over multiple panels.

the onset of auroral particle events. We find that the changes in the *H* component measured by the LYR and HOR magnetometers are mostly coinciding with the S4 variations (indicated by black vertical lines in Figures 1e and 1j).

Additional three events are classified as long-lasting particle precipitation events with respect to the auroral intensity (Figures 2c, 2h, and 2m). The events of 28th October 2019 (#2), 29th October 2019 (#3), and 7th November 2019 (#5) show the same features as the long-lasting event of 24th October 2019 (#1) in Figure 1. By comparing the S4 index shown in Figures 2a, 2f, and 2k with the auroral intensity in Figures 2c, 2h, and 2m, it is clear that the elevated S4 marks the beginnings and ends of intervals of increased auroral emission intensity. This can be seen for the S4 peak at 18:28 UT and 19:00 UT on 28th October 2019 (#2)(2a) and in relation to the auroral intensity fading at 18:25 and 18:55 UT (Figure 2c). The IFLC (Figures 2b, 2g, and 2l) and S4 index correlate for times of elevated S4 index, see for example, 18:25 UT, 18:35 UT and 18:55 UT on 28th October 2019 (#2). However, the IFLC can be noisy at times (Figure 2g at 18:30 UT–18:45 UT on 29th October 2019 (#3)). σ_ϕ variations (Figures 2d, 2i, and 2n) are present for all occasions of elevated S4. The *H* component of the magnetic field (Figures 2e, 2j, and 2o) shows variations at the onset of aurora.

A second short-lived auroral particle precipitation event is shown in Figure 3. Just like the event of 6th November 2019 (#4) shown in Figure 1, it shares the characteristics of having multiple short intense peaks in the auroral emission intensity, (Figure 3c), co-located with the spikes in S4 (Figure 3a). While for the long-lasting events, the S4 index is elevated at intensity gradients, mainly marking the beginning and end of the auroral precipitation, for the short-lasting events the precipitation can be intense and elevate the S4 index almost simultaneously. The *H* component (Figure 3e) again shows simultaneous decreases as the auroral intensity spikes. Most S4 peaks are accompanied by elevated IFLC and σ_ϕ index.

10.1029/2023SW003605

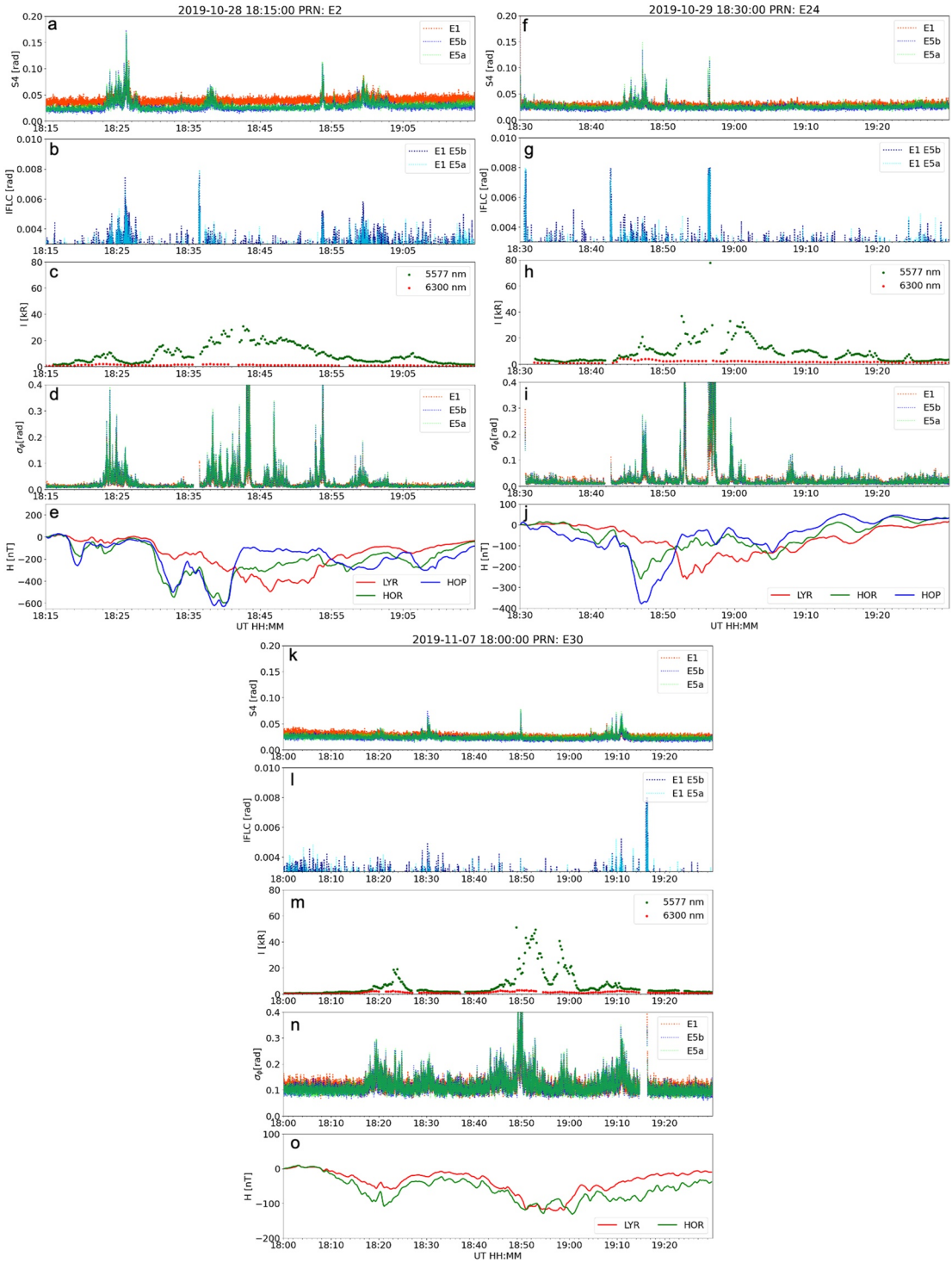

Figure 2. Small-scale plasma structures during long-lasting auroral particle precipitation. The data from 28th October 2019 (#2), 29th October 2019 (#3) and 7th November 2019 (#5) show observations of scintillation indices (S4—panel a, f, and k; σ_ϕ—panel d, i, and n), the IFLC (panel b, g, and l), magnetometer data (panel e, j, and o) and auroral intensity (panel c, h, and m). The peaks in S4 and IFLC mark strong intensity gradients (e.g., commence and end) of the elevated auroral intensity during strongly negative *H*. This suggests small-scale structuring during the commence and fading of particle precipitation. Most S4 peaks are accompanied by elevated σ_ϕ, indicating simultaneous large and small-scale structuring.

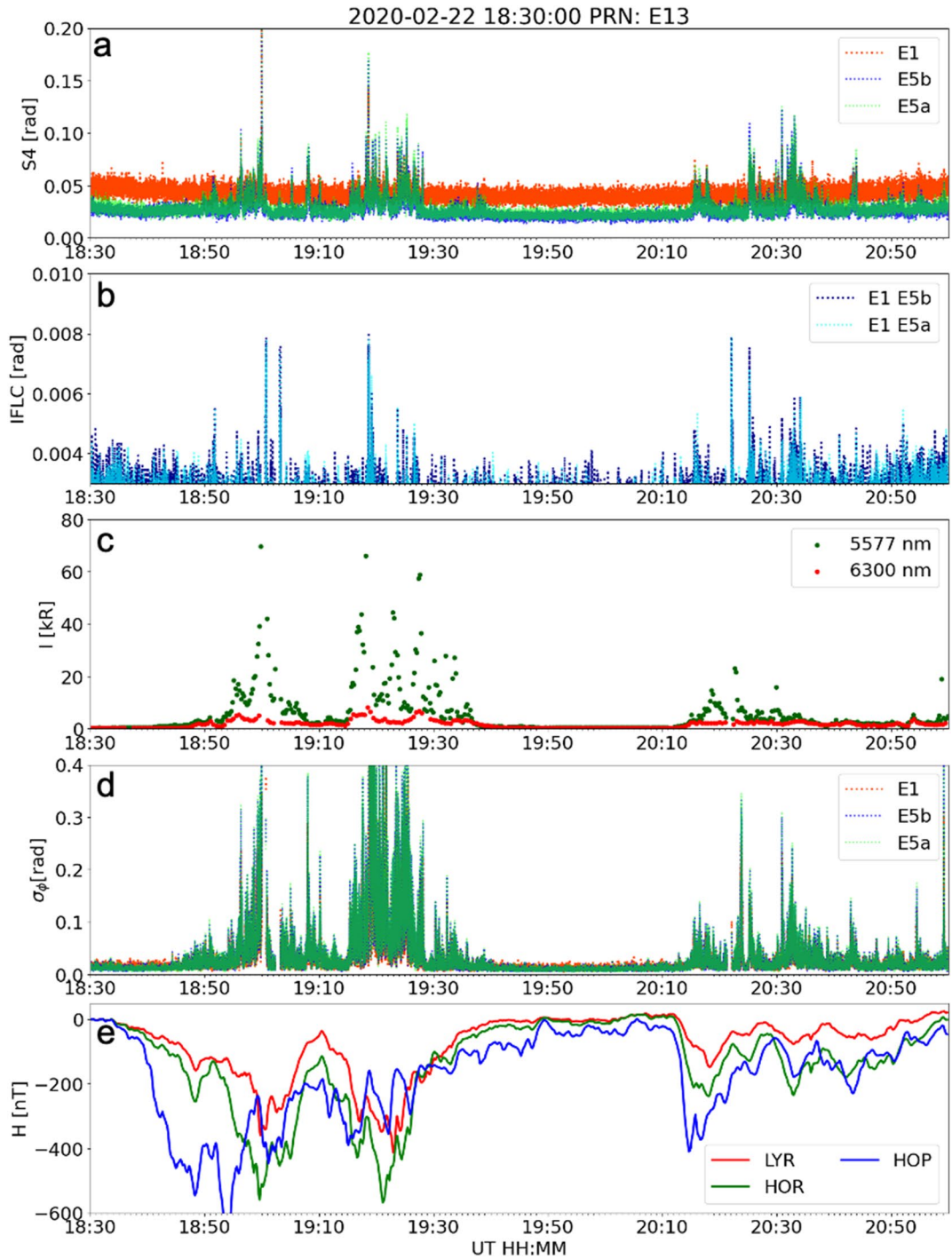

Figure 3. Small-scale plasma structures during short-lived aurora particle precipitation event. The data from 22th February 2020 show observations of scintillation indices (S4—panel a; σ_ϕ—panel d), the IFLC (panel b), magnetometer data (panel e) and auroral intensity (panel c). The peaks in S4 and IFLC mark strong intensity gradients of the elevated auroral intensity during strongly negative H. This suggests small-scale structuring at large intensity gradients of particle precipitation. Most S4 peaks are accompanied by elevated σ_ϕ, indicating simultaneous large and small-scale structuring.

To understand small-scale structuring in a spatial-temporal context, the ionospheric piercing points of the signal path of the satellites are projected onto the auroral all-sky images, see Figures 4 and 5. At two occasions the satellite PRN E30 passes through a boundary of auroral precipitation (Figures 4a and 4c) into weaker emissions/background ionosphere (Figures 4b and 4d). The auroral intensity at the ionospheric piercing point of the signal

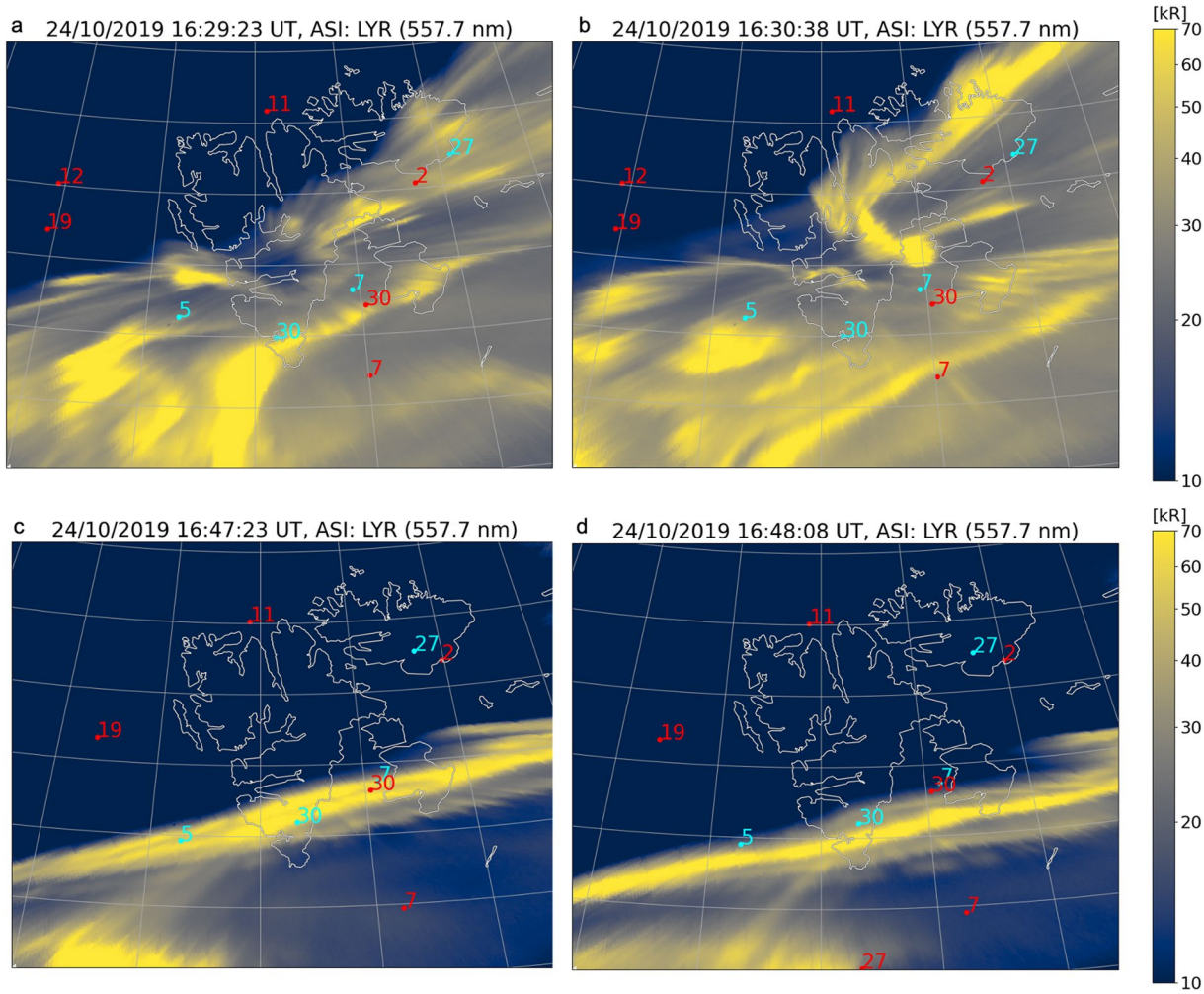

Figure 4. Spatial evolution of auroral particle precipitation and small-scale structuring at the satellite signal path piercing points. The Figure shows all-sky images and GNSS positions relative to another projected onto 150 km altitude together with a map of Svalbard. The spatial evolution remains the same as for azimuth/elevation skyplots, as shown in Supporting Information S1 (Figure S1, skyplot for 24th October 2019 (#1) 16:30:38). Intense yellow corresponds to strong auroral intensity. GPS satellite signal path piercing points are shown in cyan, Galileo satellite signal path piercing points are shown in red. Two incidents on 24th October 2019 (#1) of satellite PRN E30 passing through strong auroral emissions with a strong consequent response in increased S4 index values indicating small-scale structuring. The evolution of the scintillation indices, H-component, auroral intensity and IFLC for this event are shown in Figures 1a–1e. The auroral intensity is peaking at 16:29 UT and 16:47 UT as shown in panels (a) and (c). And after that, we observe elevated S4 index at 16:30 and 16:48 UT at low auroral intensity, see panels (b and d). Elevated S4 indices are observed at the auroral intensity gradients.

path of PRN E30 is peaking at 16:29:23 UT (Figure 4a) and 16:47:23 UT (Figure 4c), see also Figure 1c. The S4 index is peaking at 16:30:38 and 16:48:08 UT, see Figures 1a, 4b, and 4d. This happens at the same time as PRN E30 is crossing an auroral intensity gradient into weak auroral emissions (Figure 4b)/or even no auroral emissions (Figure 4d). Small-scale structures are observed at auroral intensity gradients. The evolution of the scintillation indices, *H* component of the magnetic field, auroral intensity and IFLC for this event are shown in Figures 1a–1e. The auroral intensity is peaking at 16:29 UT and 16:47 UT as shown in panels a and c. And after that, we observe elevated S4 index at 16:30 and 16:48 UT at low auroral intensity, see panels b and d. Elevated S4 indices are observed at the auroral intensity gradients.

Auroral particle precipitation crossing over piercing points of the signal path of multiple satellites is shown in Figure 5. At 19:17:23 UT PRN G24 is outside the auroral form (Figure 5a) and shows no elevated S4 (Figure 5e). As the auroral form moves poleward, the signal of PRN G24 travels through an intensity gradient (Figures 5b and 5c). The S4 index onsets at about 19:18 UT after the signal is passing through the intensity gradient (Figures 5d and 5e). PRN E1 is within strong auroral emissions at 19:17 UT, see Figure 5a. The S4 index is elevated latest at 19:17:38 UT (Figures 1f and 5b), and stays elevated at 19:17:53 UT (Figures 1f and 5c). However at 19:18 UT

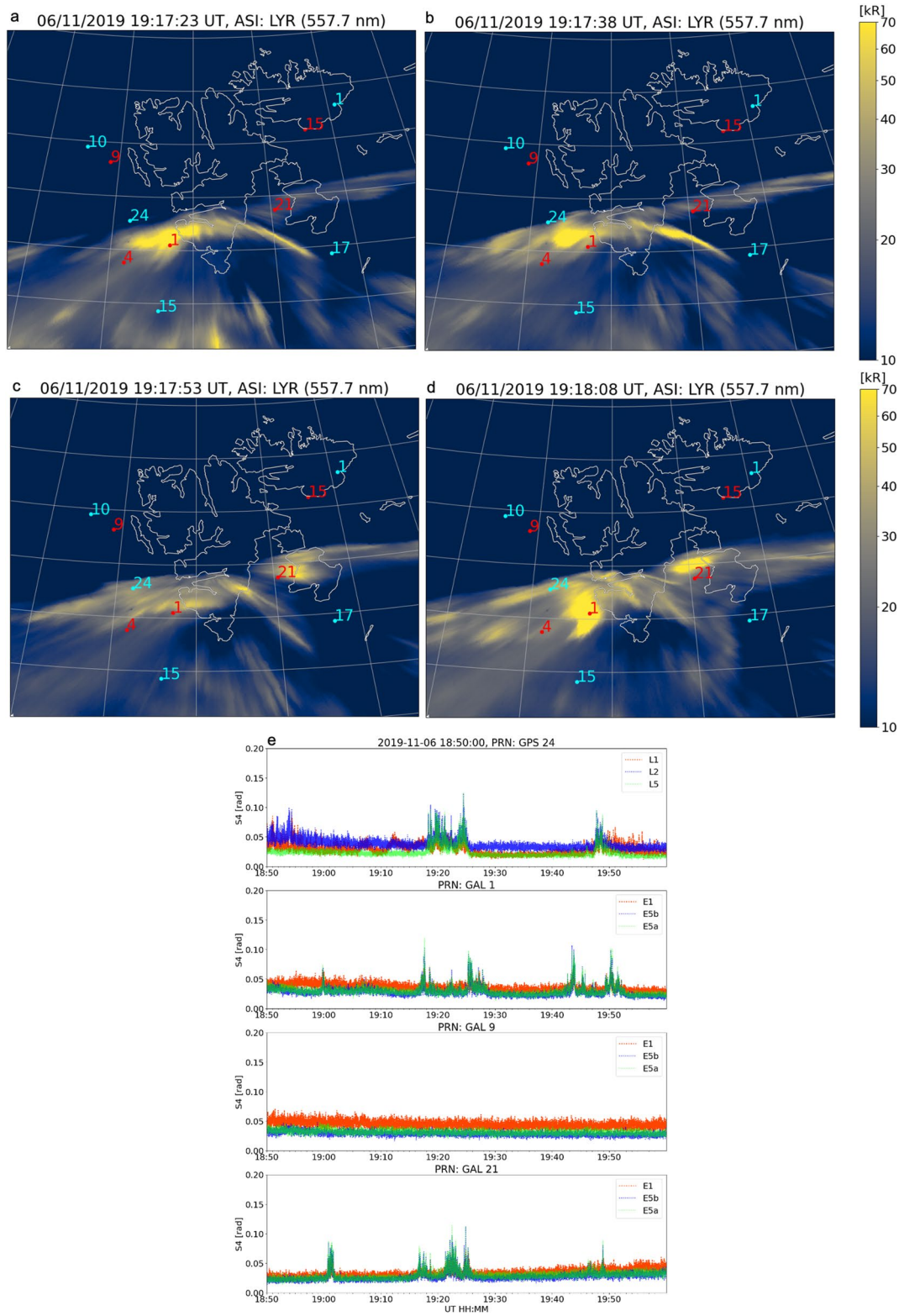

Figure 5. Auroral particle precipitation over four different satellite signal path ionospheric piercing points (PRN GPS 24, E1, E9, and E21). Panels (a–d) show GNSS positions and all-sky images projected to 150 km altitude together with a map of Svalbard. Intense yellow corresponds to strong auroral intensity. GPS satellite signal path ionospheric piercing points are shown in cyan, Galileo satellite signal path ionospheric piercing points are shown in red. The S4 index variations from 18:50 UT to 20:00 UT are shown in panel (e) for the satellites PRN G24, E1, E9, and E21. Elevated S4 indices are observed for PRN G24, E1, and E21 coinciding with the particle precipitation gradient. PRN E9 does not pass through auroral precipitation and observes no small-scale plasma structuring.

when PRN E1 is at the center of high auroral intensity emissions (Figure 5d), the S4 index has returned to a local minimum before the next peak. PRN E9 does not pass through any auroral emissions in the investigated time window and does not show any elevated S4 variations (Figures 5a–5d and 5g). The S4 index of PRN E21 shows multiple spikes between 19:17 UT and 19:18 UT, Figures 5a–5d, while it sits on a changing gradient of auroral intensity. Again, small-scale structures are observed at the auroral intensity gradients.

4. Discussion

We have analyzed the response of the amplitude scintillation index S4, which we evaluated on a 1–s level, to the auroral particle precipitation in the evening sector 16:00 UT–21:00 UT (MLT: 19:00–24:00) over Svalbard. Six events from the 2019/2020 season were studied with data from the LYR all-sky imager and LYR GNSS receiver. They showed intense auroral emissions (above 30 kR) that corresponded were accompanied with moderate local deflections (over 100 nT) in the *H* component of the Earth's magnetic field over Svalbard for Kp > 1+. The events were sorted into two different types of the auroral particle precipitation: long-lasting (>5 min) and short-lived (<5 min).

In all observed events, the green auroral emissions peaked above 30 kR and were correlated with scintillation indices, whereas the red auroral emissions remained weak (below 10 kR). At times of elevated σ_ϕ and S4 values, the red auroral emissions are weak, whereas the green auroral emissions correspond to the σ_ϕ variations. This suggests that in particular the E-region plasma processes and instabilities driven by the auroral particle precipitation resulting in green emissions may lead to small- and large-scale plasma structuring that impact radio waves at GNSS frequencies. In the following, we will focus on the green auroral emissions in relation to the derived scintillation indices.

For the long-lasting events, multiple peaks were observed in the S4 index indicating the beginning and end of emissions, and the intensity gradients. On 24th October 2019 (#1), the onset at 16:15 UT and fading at 16:47 UT of the particle precipitation are reflected in the S4 index increases, and so is the sharp auroral intensity increase at 16:29 UT, see again Figures 1a and 1c. The particle precipitation during the event on 28th October 2019 (#2) commences at 18:22 UT, a sharp increase in the auroral intensity is also noted at 18:36 UT and the intensity decrease is gradual after 18:53. All of these times are accompanied by S4 index increases, see again Figures 2a and 2c. The third long-lasting particle precipitation event on 29th October 2019 (#3) shows a particle precipitation onset at 18:45 UT correlated with S4 index variations. During the event, the auroral intensity peaks around 18:57 UT and with it the S4 index, see again Figures 2f and 2h. No variations of the S4 index are found at the fading of the precipitation in this event. The event on 7th November 2019 (#5) shows an increase in the S4 index at its abrupt start at 18:50 UT, and the S4 index varies after 19:03 UT and at 19:10 UT as the intensity is fading. A shorter, just above 5-min long event is shown at 18:20–18:30 UT with an elevated S4 index marking its beginning and end, see again Figures 2k and 2m.

The short-lived events show similar signatures of correlated precipitation and S4 index as the long-lasting events. However, as they are short, the S4 index variations do not cease during the event. When the precipitation declines or moves, it will still take some time for the plasma structures to diffuse. During this "memory effect," instabilities will further structure plasma and dissipate energy (Enengl et al., 2023). On 6th November 2019 (#4), multiple peaks in the auroral intensity (19:00 UT, 19:18 UT, 19:22 UT, 19:26 UT, 19:44 UT, 19:50 UT) are correlated with the peaks in the S4 index, see again Figures 1f and 1h. As the onset and fading happen in 1–5 min intervals, the S4 index shows continuous variations in response. On 22nd February 2020 (#6), there were multiple short-lived auroral emission peaks that were close to one another between 19:10 UT and 19:40 UT when the satellite signal was subject to intensification of the S4 index above the noise level. The same can be observed for the other peaks (18:58 UT, 20:30 UT) in the investigated time window, see again Figures 3a and 3c.

A correspondence between the IFLC and S4 index can be observed for most of the above listed elevated S4 index variations related to auroral particle precipitation, when there is low noise in the IFLC values (all events except 24th October 2019 (#1) at 16:00–16:20 UT), see Figures 1–3- S4 and IFLC.

During all above listed elevated S4 index variations, we find elevated σ_ϕ values. This means that we find small-scale plasma structuring accompanied with larger scale plasma structuring. The σ_ϕ index magnitude, however, is not a measure to predict the S4 index magnitudes. Some σ_ϕ variations do not correspond to any S4 variations, such as on 24th October 2019 (#1) at 16:35 UT (Figure 1d) and 28th October 2019 (#2) at 18:40 UT (Figure 2d). The

σ_ϕ index can also be elevated during long-lasting events, while the S4 index is specifically elevated at auroral intensity gradients.

Sharp decreases in the *H* component of the Earth's magnetic field are found in relation to the S4 index increases. However, as the receiver to satellite line-of-sight is at a distance to the magnetometer stations, there is a delay between the observed *H* decreases and the S4 increases, see again Figures 1–3 panels for the *H* component of the magnetic field. This indicates that particle precipitation is jointly responsible for the observed plasma structuring down to the Fresnel scale, resulting in increased S4 on a 1-s time scale, and for the increased conductivity, intensifying the auroral electrojet, as illustrated by the related decrease of the *H* component of the Earth's magnetic field.

Comparing the spatial evolution of the auroral emissions with the satellite signal path ionospheric piercing points and elevated S4 index (Figures 4 and 5) confirms that elevated S4 indices are found near auroral emission gradients. The highest S4 values are located at the edges of auroral forms (when the signal path ionospheric piercing point is moving in/out of the auroral form) or at local intensification or weakening of auroral precipitation along the line of sight. In short, elevated S4 indices are observed at or after auroral intensity gradients along the line of sight from the satellite to the receiver.

In summary: (a) Elevated S4 values are associated with auroral intensity gradients as different levels of particle precipitation pass through the line of sight of the satellite to the receiver. (b) The IFLC often corresponds to increases of S4 index variations. (c) Intensification of ionospheric currents contributes to Fresnel-scale structuring.

In the following, we interpret the observations in terms of ionospheric plasma processes and the impacts on trans-ionospheric radio wave propagation.

During ionosphere-magnetosphere coupling, strong electric fields and currents trigger plasma instabilities that can lead to turbulence and energy dissipation in the E-region ionosphere. Thus, turbulence can lead to strong electron heating, which can increase the global ionospheric conductance (Bahcivan, 2007; Dimant & Oppenheim, 2011a, 2011b; Schlegel & St.-Maurice, 1981). The E-region ionospheric plasma is subject to energetic particle beams from the particle precipitation and to collisions with available neutrals. Particle precipitation into the ionospheric E-region leads to a widespread irregularities and energy dissipation, and it plays a main role in E-region large-scale ionospheric plasma structuring (Enengl et al., 2023; Makarevich et al., 2021).

Both, short-lived and long-lasting particle precipitation events, show the same response of S4 index variations to precipitation, namely elevated S4 values linked to auroral intensity gradients. Auroral intensity gradients may indicate that processes at the auroral boundary, between background plasma and an energetic particle precipitation beam, contribute to small-scale plasma structuring in the E-region ionosphere.

An instability that can lead to plasma structuring in the E-region of the polar ionosphere is the Farley-Buneman instability. A necessary condition for this instability is a difference in the flow velocities between electrons and ions (Buneman, 1963; Farley Jr, 1963). It arises due different collision frequencies with neutrals for electrons and ions. While electrons remain largely magnetized and follow the $\vec{E} \times \vec{B}$ drift velocity, ions can become unmagnetized due to larger collision cross sections, and effectively get decelerated. For sufficiently large electric fields, the difference in flow speed between species is large enough for the instability to grow. Thus, the Farley-Buneman instability extracts its energy from the velocity difference between electrons and collision-affected ions (Buneman, 1963; Farley Jr, 1963). The Farley-Buneman instability may explain why the S4 index variations are present at the edges of strong particle precipitation gradients, which are related to inhomogeneities in the E-region conductance. (Note that it is also where one can expect a larger scale Kelvin-Helmholtz instability to be present due to flow shears).

Dimant et al. (2021) note that energetic electrons reaching the E-region ionosphere can modify the instability threshold of the Farley-Buneman type of instabilities. Without precipitation, strong electric fields, which are mapped down from the magnetosphere, can drive E-region instabilities, which further lead to plasma turbulence and increased conductance. Electron precipitation, however, can dramatically raise the instability threshold, and can even largely suppress the instability inside the auroral regions, due to both the effect of additional pressure and the energy dependence of the electron-neutral collision frequency. Our observations agree with Dimant et al. (2021), as we do not observe plasma structuring within auroral emissions, but we do observe plasma structuring at the boundaries of the particle precipitation signature.

E-region instabilities can cause electron heating, enhanced plasma particle transport and small-scale plasma turbulence that modifies large-scale ionospheric conductance and with it the entire dynamics of the near-Earth's plasma (Dimant et al., 2021). Our observations of co-located large-scale σ_ϕ index observations and small-scale amplitude index variations confirm the hypothesis that the E-region dynamics is affected by the auroral particle precipitation leading to large and small-scale (above and below Fresnel scale) plasma structuring.

Field-aligned currents couple the magnetosphere to the ionosphere. Particle precipitation is a signature of this phenomenon and can directly impact ionospheric plasma by structured precipitation and result in elevated scintillation index values (Boström, 1964; Carter et al., 2016; Fæhn Follestad et al., 2020; Xiong et al., 2020). In our observations, the decreases in the *H* component of the Earth magnetic field confirm geomagnetic perturbations at the onset of particle precipitation and elevated scintillation indices. We can conclude that field-aligned currents intensify, as evidenced by the enhancement of horizontal currents shown by the decrease in the H component, due to increased particle precipitation. Conversely, this increased particle precipitation also leads to plasma structuring below the Fresnel scale, as demonstrated by the simultaneous variations in scintillation indices (σ_ϕ and S4).

For the studied events, we find the IFLC variations at the same time as elevated S4 index values. Zheng et al. (2022) stated that although both, IFLC and S4, indicate diffractive variations, they are not always correlated. This is in agreement with our study, as we find IFLC correlated with S4 for most of the S4 enhancements, but not all IFLC variations are reflected in the S4 index. This may be due to high noise levels in the IFLC. The IFLC can be used as a measure for diffractive effects as the refractive part is removed. High-frequency, refractive, variations in the GPS carrier phase can be wrongly classified as scintillation, where refractive variations are deterministic and diffractive variations are stochastic (McCaffrey & Jayachandran, 2019). Care must be taken at the choice of the cutoff frequency for phase detrending or a fast iterative filtering detrending scheme can be used to provide a more realistic determination of the phase scintillation index (Ghobadi et al., 2020). We therefore carefully studied S4 and IFLC to correctly identify diffractive variations. Our results show that diffractive effects impact the signal at the onset, fading or strong changes of the auroral particle precipitation. Since σ_ϕ variations are not always found simultaneously with S4 index variations, some σ_ϕ variations can be of purely refractive nature caused by convected larger plasma structures during the particle precipitation. While at strong precipitation gradients, the σ_ϕ index also includes diffractive variations, it seems otherwise to mainly include refractive signal variations. Conroy et al. (2022) suggests that high latitude phase variations are mainly of refractive nature. As the IFLC and S4 show little to no variation during long-lasting precipitation events, they are observed as refractive and deterministic. Only at the auroral intensity gradients (e.g., beginning and end) the scintillations are classified as diffractive. For short-lasting precipitation, we find IFLC and S4 elevated, therefore they are fully classified as diffractive. In summary, we observe diffractive scintillation accompanied by amplitude scintillation during strong gradients (e.g., short-lived events, beginning and ending of long-lasting events) leading to stochastic effects.

In this article, we observe that the auroral particle precipitation can be a main driver of ionospheric irregularities leading to scintillation of radio waves. However, we note that elevated σ_ϕ, S4 and IFLC can also be detected without auroral particle precipitation. While particle precipitation is indicated as one source of plasma structuring and impacts radio wave propagation, other sources exist. Further sources can for example, be polar cap patches or auroral blobs (Jin et al., 2016; Moen et al., 2013). Further studies at high resolution (e.g., at and below 1-s averaged indices) are needed to compare different ionospheric phenomena and understand whether they lead to small-scale plasma structuring and diffractive effects on ionospheric radio wave propagation.

5. Conclusions

This paper investigated the response of the S4 index, evaluated from GNSS signals on a 1–s basis, to intense auroral particle precipitation events over Svalbard. The S4 index is a proxy for small-scale plasma structuring, which we find to be associated with intense particle precipitation. Elevated S4 index values can be observed under various conditions, even without strong auroral emissions. Here we specifically looked at strong auroral emissions in the evening sector during ongoing geomagnetic activity quantified by local deflections of the horizontal magnetic field component and combined with all-sky camera and scintillation receiver data at high latitudes (Longyearbyen, Svalbard). We identified six intense precipitation events to study the S4 response. Our results show that:

1. Clear increases in the S4 values above the noise floor level are observed at large auroral intensity gradients, as the bright aurora is moving in/out of the line of sight from the satellite to the ground receiver. The values of S4 indicate a weak scintillation activity, as S4 is never exceeding 0.2 in our study.

2. The IFLC is often elevated simultaneously with the S4 index, confirming the diffractive nature of the events.
3. Elevated σ_ϕ index can be observed without elevated S4 index or IFLC.
4. Significant increases in the auroral particle precipitation result in joint signatures of increased ionospheric currents and plasma structuring below the Fresnel's scale.

Why small-scale plasma structuring processes in the E-region are observed specifically at auroral intensity gradients remains an open question. Further statistical studies need to be carried out to investigate plasma instabilities like Farley-Buneman as a likely cause for small-scale structuring. Multi-instrument case studies, including in situ measurements by rockets and satellites, are required to understand the combination of simultaneous large-scale and small-scale structuring processes driven by auroral particle precipitation, their spatial/temporal evolution and their connection with the magnetic field geometry linked to the IMF conditions.

Data Availability Statement

The scintillation data managed by the Istituto Nazionale di Geofisica e Vulcanologia (INGV) are available at eSWua web portal (www.eswua.ingv.it), that is operated by the Upper Atmosphere Physics and Radio propagation group of INGV.

Acknowledgments
WJM, DK, and YJ acknowledge funding from the European Research Council (ERC) under the European Union's Horizon 2020 research and innovation programme (ERC Consolidator Grant agreement No. 866357, POLAR-4DSpace). This research is a part of the 4DSpace Strategic Research Initiative at the University of Oslo. KO acknowledges support from the Research Council of Norway under contract 223252. LS is grateful to Emanuele Pica and Carlo Marcocci from INGV for the support on raw GNSS data acquired by the Longyearbyen ionospheric scintillation monitor receiver. The authors are grateful to the University of Tromsø for hosting the GNSS receiver in Longyearbyen. The authors are also grateful to GRAPE (GNSS Research and Application for Polar Environment) SCAR Expert Group for supporting this study. The authors thank Bjørn Lybekk for the maintenance of the all-sky imager data.

References

Akasofu, S.-I. (1965). Dynamic morphology of auroras. *Space Science Reviews*, *4*(4), 498. https://doi.org/10.1007/BF00177092

Alfonsi, L., Bergeot, N., Cilliers, P. J., De Franceschi, G., Baddeley, L., Correia, E., et al. (2022). Review of environmental monitoring by means of radio waves in the polar regions: From atmosphere to geospace. *Surveys in Geophysics*, *43*(6), 1609–1698. https://doi.org/10.1007/s10712-022-09734-z

Alfonsi, L., Spogli, L., De Franceschi, G., Romano, V., Aquino, M., Dodson, A., & Mitchell, C. N. (2011). Bipolar climatology of GPS ionospheric scintillation at solar minimum. *Radio Science*, *46*(03), 1–21. https://doi.org/10.1029/2010RS004571

Bahcivan, H. (2007). Plasma wave heating during extreme electric fields in the high-latitude E region. *Geophysical Research Letters*, *34*(15), L15106. https://doi.org/10.1029/2006GL029236

Basu, S., Basu, S., Costa, E., Bryant, C., Valladares, C. E., & Livingston, R. C. (1991). Interplanetary magnetic field control of drifts and anisotropy of high-latitude irregularities. *Radio Science*, *26*(4), 1079–1103. https://doi.org/10.1029/91RS00586

Basu, S., Weber, E. J., Bullett, T. W., Keskinen, M. J., MacKenzie, E., Doherty, P., et al. (1998). Characteristics of plasma structuring in the cusp/cleft region at Svalbard. *Radio Science*, *33*(6), 1885–1899. https://doi.org/10.1029/98RS01597

Beach, T. L. (2006). Perils of the GPS phase scintillation index ($\sigma\varphi$). *Radio Science*, *41*(5), 1–7. https://doi.org/10.1029/2005RS003356

Boström, R. (1964). A model of the auroral electrojets. *Journal of Geophysical Research*, *69*(23), 4983–4999. https://doi.org/10.1029/JZ069i023p04983

Bougard, B., Sleewaegen, J., Spogli, L., Veettil, S. V., & Monico, J. (2011). CIGALA: Challenging the solar maximum in Brazil with PolaRxS. In *Proceedings of the 24th international technical meeting of the satellite division of the institute of navigation (ion GNSS 2011)* (pp. 2572–2579).

Brekke, A. (2013). *Physics of the upper polar atmosphere*. Springer. https://doi.org/10.1007/978-3-642-27401-5

Briggs, B., & Parkin, I. (1963). On the variation of radio star and satellite scintillations with zenith angle. *Journal of Atmospheric and Terrestrial Physics*, *25*(6), 339–366. https://doi.org/10.1016/0021-9169(63)90150-8

Buneman, O. (1963). Excitation of field aligned sound waves by electron streams. *Physical Review Letters*, *10*(7), 285–287. https://doi.org/10.1103/PhysRevLett.10.285

Carrano, C. S., Groves, K. M., McNeil, W. J., & Doherty, P. H. (2013). Direct measurement of the residual in the ionosphere-free linear combination during scintillation. In *Proceedings of the 2013 international technical meeting of the institute of navigation* (pp. 585–596).

Carter, J. A., Milan, S. E., Coxon, J. C., Walach, M.-T., & Anderson, B. J. (2016). Average field-aligned current configuration parameterized by solar wind conditions. *Journal of Geophysical Research: Space Physics*, *121*(2), 1294–1307. https://doi.org/10.1002/2015JA021567

Cicone, A. (2020). Iterative filtering as a direct method for the decomposition of nonstationary signals. *Numerical Algorithms*, *85*(3), 811–827. https://doi.org/10.1007/s11075-019-00838-z

Cicone, A., & Zhou, H. (2021). Numerical analysis for iterative filtering with new efficient implementations based on FFT. *Numerische Mathematik*, *147*, 1–28. https://doi.org/10.1007/s00211-020-01165-5

Conroy, J. P., Deshpande, K., Scales, W., & Zaghloul, A. (2022). Statistical analysis of refractive and diffractive scintillation at high latitudes. *Radio Science*, *57*(2), e2021RS007259. https://doi.org/10.1029/2021RS007259

Cordes, J. M., Pidwerbetsky, A., & Lovelace, R. V. E. (1986). Refractive and diffractive scattering in the interstellar medium. *The Astrophysical Journal*, *310*, 737. https://doi.org/10.1086/164728

Dahlgren, H., Schlatter, N. M., Ivchenko, N., Roth, L., Karlsson, A., Dahlgren, H., & Karlsson, A. (2017). Relation of anomalous F region radar echoes in the high-latitude ionosphere to auroral precipitation. *Annales Geophysicae*, *35*(3), 475–479. https://doi.org/10.5194/angeo-35-475-2017

De Franceschi, G., Spogli, L., Alfonsi, L., Romano, V., Cesaroni, C., & Hunstad, I. (2019). The ionospheric irregularities climatology over Svalbard from solar cycle 23. *Scientific Reports*, *9*(1), 9232. https://doi.org/10.1038/s41598-019-44829-5

de Paula, E. R., Martinon, A. R. F., Moraes, A. O., Carrano, C., Neto, A. C., Doherty, P., et al. (2021). Performance of 6 different global navigation satellite system receivers at low latitude under moderate and strong scintillation. *Earth and Space Science*, *8*(2). https://doi.org/10.1029/2020EA001314

Dimant, Y. S., Khazanov, G. V., & Oppenheim, M. M. (2021). Effects of electron precipitation on E-region instabilities: Theoretical analysis. *Journal of Geophysical Research: Space Physics*, *126*(12), e2021JA029884. https://doi.org/10.1029/2021JA029884

Dimant, Y. S., & Oppenheim, M. M. (2011a). Magnetosphere-ionosphere coupling through E region turbulence: 1. Energy budget. *Journal of Geophysical Research*, *116*(A9), A09303. https://doi.org/10.1029/2011JA016648

Dimant, Y. S., & Oppenheim, M. M. (2011b). Magnetosphere-ionosphere coupling through E region turbulence: 2. Anomalous conductivities and frictional heating. *Journal of Geophysical Research*, *116*(A9), A09304. https://doi.org/10.1029/2011JA016649
D'Onofrio, M., Partamies, N., & Tanskanen, E. (2014). Eastward electrojet enhancements during substorm activity. *Journal of Atmospheric and Solar-Terrestrial Physics*, *119*, 129–137. https://doi.org/10.1016/j.jastp.2014.07.007
Enengl, F., Kotova, D., Jin, Y., Clausen, L. B., & Miloch, W. J. (2023). Ionospheric plasma structuring in relation to auroral particle precipitation. *Journal of Space Weather and Space Climate*, *13*, 1. https://doi.org/10.1051/swsc/2022038
Fæhn Follestad, A., Herlingshaw, K., Ghadjari, H., Knudsen, D. J., McWilliams, K. A., Moen, J. I., et al. (2020). Dayside field-aligned current impacts on ionospheric irregularities. *Geophysical Research Letters*, *47*(11), e2019GL086722. https://doi.org/10.1029/2019GL086722
Farley, D. T., Jr. (1963). A plasma instability resulting in field-aligned irregularities in the ionosphere. *Journal of Geophysical Research*, *68*(22), 6083–6097. https://doi.org/10.1029/JZ068i022p06083
Forte, B. (2005). Optimum detrending of raw GPS data for scintillation measurements at auroral latitudes. *Journal of Atmospheric and Solar-Terrestrial Physics*, *67*(12), 1100–1109. https://doi.org/10.1016/j.jastp.2005.01.011
Forte, B., & Radicella, S. M. (2002). Problems in data treatment for ionospheric scintillation measurements. *Radio Science*, *37*(6), 1–5. https://doi.org/10.1029/2001RS002508
Fremouw, E., Leadabrand, R., Livingston, R., Cousins, M., Rino, C., Fair, B., & Long, R. (1978). Early results from the DNA wideband satellite experiment—Complex-signal scintillation. *Radio Science*, *13*(1), 167–187. https://doi.org/10.1029/RS013i001p00167
Ghobadi, H., Spogli, L., Alfonsi, L., Cesaroni, C., Cicone, A., Linty, N., et al. (2020). Disentangling ionospheric refraction and diffraction effects in GNSS raw phase through fast iterative filtering technique. *GPS Solutions*, *24*(3), 85. https://doi.org/10.1007/s10291-020-01001-1
Greenwald, R. A., Shepherd, S. G., Sotirelis, T. S., Ruohoniemi, J. M., & Barnes, R. J. (2002). Dawn and dusk sector comparisons of small-scale irregularities, convection, and particle precipitation in the high-latitude ionosphere. *Journal of Geophysical Research*, *107*(A9), SIA1-1–SIA1-12. https://doi.org/10.1029/2001JA000158
Hey, J. S., Parsons, S. J., & Phillips, J. W. (1946). Fluctuations in cosmic radiation at radio-frequencies. *Nature (London)*, *158*(4007), 234. https://doi.org/10.1038/158234a0
Huba, J. D., Hassam, A. B., Schwartz, I. B., & Keskinen, M. J. (1985). Ionospheric turbulence: Interchange instabilities and chaotic fluid behavior. *Geophysical Research Letters*, *12*(1), 65–68. https://doi.org/10.1029/GL012i001p00065
Jin, Y., Moen, J. I., Miloch, W. J., Clausen, L. B. N., & Oksavik, K. (2016). Statistical study of the GNSS phase scintillation associated with two types of auroral blobs. *Journal of Geophysical Research: Space Physics*, *121*(5), 4679–4697. https://doi.org/10.1002/2016JA022613
Kashcheyev, A., Nava, B., & Radicella, S. M. (2012). Estimation of higher-order ionospheric errors in GNSS positioning using a realistic 3-D electron density model. *Radio Science*, *47*(4). https://doi.org/10.1029/2011RS004976
Keskinen, M. J., & Ossakow, S. L. (1983). Theories of high-latitude ionospheric irregularities: A review. *Radio Science*, *18*(6), 1077–1091. https://doi.org/10.1029/RS018i006p01077
King, J., & Papitashvili, N. (2005). Solar wind spatial scales in and comparisons of hourly wind and ace plasma and magnetic field data. *Journal of Geophysical Research*, *A02104*(A2), 110. https://doi.org/10.1029/2004JA010649
Kintner, P. M., Ledvina, B. M., & de Paula, E. R. (2007). GPS and ionospheric scintillations. *Space Weather*, *5*(9), S09003. https://doi.org/10.1029/2006SW000260
Kintner, P. M., & Seyler, C. E. (1985). The status of observations and theory of high latitude ionospheric and magnetospheric plasma turbulence. *Space Science Reviews*, *41*(1–2), 91–129. https://doi.org/10.1007/BF00241347
Kropotkin, A. (2016). Formation of the small-scale structure of auroral electron precipitations. *Journal of Atmospheric and Solar-Terrestrial Physics*, *148*, 39–47. https://doi.org/10.1016/j.jastp.2016.08.009
Makarevich, R. A., Crowley, G., Azeem, I., Ngwira, C., & Forsythe, V. V. (2021). Auroral E-region as a source region for ionospheric scintillation. *Journal of Geophysical Research: Space Physics*, *126*(5), e2021JA029212. https://doi.org/10.1029/2021JA029212
Materassi, M., & Mitchell, C. N. (2007). Wavelet analysis of GPS amplitude scintillation: A case study. *Radio Science*, *42*(01), 1–10. https://doi.org/10.1029/2005RS003415
McCaffrey, A. M., & Jayachandran, P. T. (2019). Determination of the refractive contribution to GPS phase "scintillation". *Journal of Geophysical Research: Space Physics*, *124*(2), 1454–1469. https://doi.org/10.1029/2018JA025759
Moen, J. I., Oksavik, K., Alfonsi, L., Dåbakk, Y. R., Romano, V., & Spogli, L. (2013). Space weather challenges of the polar cap ionosphere. https://doi.org/10.1051/swsc/2013025
Mrak, S., Coster, A. J., Groves, K., & Nikoukar, R. (2023). Ground-based infrastructure for monitoring and characterizing intermediate-scale ionospheric irregularities at mid-latitudes. *Frontiers in Astronomy and Space Sciences*, *10*. https://doi.org/10.3389/fspas.2023.1091340
Oksavik, K., van der Meeren, C., Lorentzen, D. A., Baddeley, L. J., & Moen, J. (2015). Scintillation and loss of signal lock from poleward moving auroral forms in the cusp ionosphere. *Journal of Geophysical Research: Space Physics*, *120*(10), 9161–9175. https://doi.org/10.1002/2015JA021528
Partamies, N., Whiter, D., Kauristie, K., & Massetti, S. (2022). Magnetic local time (MLT) dependence of auroral peak emission height and morphology. *Annales Geophysicae*, *40*(5), 605–618. https://doi.org/10.5194/angeo-40-605-2022
Rino, C., Morton, Y., Breitsch, B., & Carrano, C. (2019). Stochastic TEC structure characterization. *Journal of Geophysical Research: Space Physics*, *124*(12), 10571–10579. https://doi.org/10.1029/2019ja026958
Rogister, A., & D'Angelo, N. (1970). Type II irregularities in the equatorial electrojet. *Journal of Geophysical Research*, *75*(19), 3879–3887. https://doi.org/10.1029/JA075i019p03879
Schlegel, K., & St.-Maurice, J. P. (1981). Anomalous heating of the polar E region by unstable plasma waves 1. observations. *Journal of Geophysical Research*, *86*(A3), 1447–1452. https://doi.org/10.1029/JA086iA03p01447
Semeter, J., Mrak, S., Hirsch, M., Swoboda, J., Akbari, H., Starr, G., et al. (2017). GPS signal corruption by the discrete aurora: Precise measurements from the mahali experiment. *Geophysical Research Letters*, *44*(19), 9539–9546. https://doi.org/10.1002/2017GL073570
Smith, A. M., Mitchell, C. N., Watson, R. J., Meggs, R. W., Kintner, P. M., Kauristie, K., & Honary, F. (2008). GPS scintillation in the high Arctic associated with an auroral arc. *Space Weather*, *6*(3). https://doi.org/10.1029/2007SW000349
Spogli, L., Alfonsi, L., De Franceschi, G., Romano, V., Aquino, M., & Dodson, A. (2009). Climatology of GPS ionospheric scintillations over high and mid-latitude European regions. In *Annales geophysicae* (Vol. 27, pp. 3429–3437). https://doi.org/10.5194/angeo-27-3429-2009
Spogli, L., Ghobadi, H., Cicone, A., Alfonsi, L., Cesaroni, C., Linty, N., et al. (2021). Adaptive phase detrending for GNSS scintillation detection: A case study over Antarctica. *IEEE Geoscience and Remote Sensing Letters*, *19*, 1–5. https://doi.org/10.1007/s10291-020-01001-1
Tanskanen, E. (2009). A comprehensive high-throughput analysis of substorms observed by image magnetometer network: Years 1993-2003 examined. *Journal of Geophysical Research*, *114*(A5), A05204. https://doi.org/10.1029/2008JA013682
Treumann, R. A. (1997). *Advanced space plasma physics*. Imperial College Press. https://doi.org/10.1142/p020

Upper atmosphere physics and radiopropagation Working Group, Cesaroni, C., Marcocci, C., Pica, E., & Spogli, L. (2020). *Electronic space weather upper atmosphere database (eSWua)—total electron content (TEC) data, version 1.0*. Istituto Nazionale di Geofisica e Vulcanologia (INGV). https://doi.org/10.13127/ESWUA/TEC

Urbar, J., Spogli, L., Cicone, A., Clausen, L. B., Jin, Y., Wood, A. G., et al. (2022). Multi-scale response of the high-latitude topside ionosphere to geospace forcing. *Advances in Space Research*, *72*(12), 5490–5502. https://doi.org/10.1016/j.asr.2022.06.045

van der Meeren, C., Oksavik, K., Lorentzen, D. A., Rietveld, M. T., & Clausen, L. B. N. (2015). Severe and localized GNSS scintillation at the poleward edge of the nightside auroral oval during intense substorm aurora. *Journal of Geophysical Research: Space Physics*. https://doi.org/10.1002/2015JA021819

Van Dierendonck, A. J., Klobuchar, J., & Hua, Q. (1993). Ionospheric scintillation monitoring using commercial single frequency C/A code receivers. *Proceedings of ION GPS-*, *93*, 1333–1342.

Wang, Y., Cao, Z., Xing, Z.-Y., Zhang, Q.-H., Jayachandran, P. T., Oksavik, K., et al. (2021). GPS scintillations and TEC variations in association with a polar cap arc. *Journal of Geophysical Research: Space Physics*, *126*(3), e2020JA028968. https://doi.org/10.1029/2020JA028968

Wang, Y., Jayachandran, P., Ma, Y.-Z., Zhang, Q.-H., Xing, Z.-Y., Ruohoniemi, J., et al. (2022). Dependencies of GPS scintillation indices on the ionospheric plasma drift and rate of change of TEC around the dawn sector of the polar ionosphere. *Journal of Geophysical Research: Space Physics*, *127*(11), e2022JA030870. https://doi.org/10.1029/2022JA030870

Wang, Y., Zhang, Q.-H., Jayachandran, P., Moen, J., Xing, Z.-Y., Chadwick, R., et al. (2018). Experimental evidence on the dependence of the standard GPS phase scintillation index on the ionospheric plasma drift around noon sector of the polar ionosphere. *Journal of Geophysical Research: Space Physics*, *123*(3), 2370–2378. https://doi.org/10.1002/2017JA024805

Wernik, A., Secan, J., & Fremouw, E. (2003). Ionospheric irregularities and scintillation. *Advances in Space Research*, *31*(4), 971–981. https://doi.org/10.1016/S0273-1177(02)00795-0

Whiter, D. K., Partamies, N., Gustavsson, B., & Kauristie, K. (2023). The altitude of green OI 557.7 nm and blue N_2^+ 427.8 nm aurora. *Annales Geophysicae*, *41*(1), 1–12. https://doi.org/10.5194/angeo-41-1-2023

Xiong, C., Stolle, C., Alken, P., & Rauberg, J. (2020). Relationship between large-scale ionospheric field-aligned currents and electron/ion precipitations: DMSP observations. *Earth Planets and Space*, *72*(1), 1–22. https://doi.org/10.1186/s40623-020-01286-z

Yeh, K. C., & Liu, C.-H. (1982). Radio wave scintillations in the ionosphere. *Proceedings of the IEEE*, *70*(4), 324–360. https://doi.org/10.1109/PROC.1982.12313

Zheng, Y., Xiong, C., Jin, Y., Liu, D., Oksavik, K., Xu, C., et al. (2022). The refractive and diffractive contributions to GPS signal scintillation at high latitudes during the geomagnetic storm on 7-8 September 2017. *Journal of Space Weather and Space Climate*, *12*, 40. https://doi.org/10.1051/swsc/2022036

Zou, S., Moldwin, M. B., Nicolls, M. J., Ridley, A. J., Coster, A. J., Yizengaw, E., et al. (2013). Electrodynamics of the high-latitude trough: Its relationship with convection flows and field-aligned currents. *Journal of Geophysical Research: Space Physics*, *118*(5), 2565–2572. https://doi.org/10.1002/jgra.50120